Development of irradiation tolerant tungsten alloys for high temperature nuclear applications

Dmitry Terentyev[1], Petra Jenus[2], Elisa Sal[3,4], Alexander Zinovev[1], Chih-Chen Chang[1,5], Carmen Garcia-Rosales[3,4], Matej Kocen[2], Saša Novak[2] , W. Van Renterghem[1]

[1]Institute for Nuclear Materials Science, SCK CEN, Boeretang 200, 2400 Mol, Belgium
[2] Jožef Stefan Institute, Jamova c39, 1000 Ljubljana, Slovenia
[3]CEIT-Basque Research and Technology Alliance (BRTA), Paseo de Manuel Lardizabal 15, 20018 San Sebastian, Spain
[4]University of Navarra, Tecnun, Paseo de Manuel Lardizabal 13, 20018 San Sebastian, Spain
[5]Institute of Mechanics, Materials and Civil Engineering (iMMC), UCLouvain, Av. Georges Lemaître 4, 1348 Louvain-la-Neuve, Belgium

ABSTRACT

Development of refractory metals for application as plasma-facing armour material remains among priorities of fusion research programmes in Europe, China and Japan. Improving the resistance to high temperature recrystallization, enhancing material strength to sustain thermal fatigue cracking and tolerance to neutron irradiation are the key indicators used for the down selection of materials and manufacturing processes to be applied to deliver engineering materials.

In this work we investigate the effect of neutron irradiation on mechanical properties and microstructure of several tungsten grades recently developed. Neutron irradiation campaign is arranged for screening purposes and therefore is limited to the fluence relevant for the ITER plasma facing components. At the same time, the neutron exposure covers a large span of irradiation temperatures from 600 up to 1000 °C. Four different grades are included in the study, namely: fine-grain tungsten strengthened by W-carbide (W-4wt.% W_2C), fine-grain tungsten strengthened by Zr carbides (W-0.5% ZrC), W alloyed with 10 at.% chromium and 0.5 at.% yttrium (W-10Cr-0.5Y) and technologically pure W plate manufactured according to the ITER specification by Plansee (Austria). The strengthening by W_2C and ZrC particles leads to an enhanced strength, moreover, the W-0.5ZrC material exhibits reduced DBTT (compared to ITER specification grade) and is available in the form of thick plate (i.e. high up-scaling potential). The W-10Cr-0.5Y grade is included as the material offering the self-passivation protection against the high temperature oxidation.

Keywords: tungsten, recrystallization, irradiation, precipitate strengthening

1. Introduction

The development and implementation of fusion power plants pledges a considerable contribution to clean and safe energy supply for future generations. To ensure the efficiency and safe operation,

extensive efforts are invested into the development of suitable structural materials, capable of withstanding the extreme conditions expected in the reactor. Although recent decades have seen substantial progress in the field of fusion-relevant materials, the development of upgraded materials remains among the priorities of fusion research programmes. The goal is to design a low-activation material capable of withstanding high heat loads in the range 10-20 MW/m^2, with sufficient mechanical and thermal properties, which must be retained even after high neutron irradiation fluence and nuclear transmutation reactions associated with the fusion nuclear environment [1-3]. Current material-oriented research focuses on the development of tungsten-based materials. They demonstrate some attractive thermo-physical properties, such as high melting point and high thermal conductivity [4-6]. However, materials' properties depend on the production route (see a parametric study of tensile properties of several tungsten grades [7, 8]). In tungsten, the most pronounced difference can be observed in brittle-to-ductile transition (DBT) temperature, which is for sintered tungsten lays in the range 400-600 °C but it can be reduced even to – 65 °C for a heavily deformed tungsten plate [9]. Similarly, there is a significant variance in a flexural strength and fracture toughness between deformed/rolled, sintered and recrystallized tungsten [10, 11].

Pure tungsten produced by conventional powder metallurgy has attractive thermo-mechanical properties, but it also has some drawbacks, such as DBTT at around 300-400 °C and recrystallization induced loss of strength, which occurs at temperatures above 1100 °C [12-15]. First issue can be solved by heavy deformation/rolling [9, 13, 14, 16, 17] by means of grain refinement and dislocations' density increase. However, tungsten is a bcc metal undergoing a recrystallization process followed by extensive grain growth. It is known that the finer the microstructure, the more pronounced recrystallization effects are [18, 19] since internal stresses initiated by the presence of deformation defects drive the recrystallization process. In order to stabilize fine-grain microstructure and to prevent grain growth, particle reinforcement by the incorporation of oxide (e.g. Y_2O_3) or carbide (e.g. TiC, TaC) particles into the W matrix was investigated [20-22]. Recently also the reinforcement of tungsten with W_2C particles was proposed [23, 24]. Particles' incorporation has proven to be effective in improvement of mechanical properties to some extent.

Another important drawback of W is its poor oxidation resistance resulting in fast oxidation at temperatures above 500 °C and significant oxide sublimation above 900 °C [15]. Under normal operation conditions, the poor oxidation resistance of W is not of concern. However, the use of pure W represents a potential safety risk in case of a loss-of-coolant accident (LOCA) with simultaneous air ingress into the vacuum vessel. In such a situation, the temperature of the first wall (FW) rises up to values of 1000 °C to almost 1200 °C, depending on the reactor design, due to the nuclear decay heat [25]. The first wall tungsten, which will be activated by neutron irradiation after the D-T plasma operation, oxidizes in the presence of air, forming volatile radioactive WO_3 with the potential release of significant amounts of highly activates species [26].

The need for new W-based materials to avoid the risk of radioactive release during such a scenario has led to the development of oxidation resistant W-based alloys. The basic idea of such alloys consists in the addition of oxide forming alloying elements into the pure W, which, in case of a LOCA with air ingress, result in the growth of a stable protective oxide layer preventing W from further oxidation. Under normal operation, the surface of these self-passivating alloys will consist of pure W due to preferential sputtering of the alloying elements by hydrogen isotopes coming from the fusion plasma.

The alloying elements of the W-based alloy used in this work are Cr and Y. This selection is based on previous works, where several W-based systems using different alloying elements have been investigated both as thin films produced by magnetron sputtering [27, 28] and as bulk alloys produced by powder metallurgy (PM) [29-33]. The W-Cr-Y system resulted in lowest oxidation rates compared to all previously manufactured alloys, while the thermo-mechanical properties of W-Cr-Y alloys remained acceptable for their use as FW armour material [30].

Overall, an important step in the development of new materials and components is validation of their improved properties after high flux neutron irradiation. It is well understood that the nuclear phase of the fusion operation is inevitably linked with the emission of 14 MeV neutrons which are then used to extract the heat by being absorbed in the plasma facing components [34]. While the dedicated neutron sources (i.e. IFMIF and DONES) are still under development [35, 36], material test reactors is the only viable option we have today to study the effect of the high flux neutron fields. Correspondingly, the irradiation of tungsten requires a dedicated design to reduce thermal neutron flux (otherwise transmutation of Re and Os exceeds the rate expected in fusion environment) as well as high irradiation temperature (considerably higher than the one for structural materials in Gen II, III and IV reactors) [37]. Such irradiation typically involves miniaturized specimens of simple geometry, tensile or bending, which enables efficient payload, good thermal control and simple handling after the irradiation. Even after relatively low irradiation doses, say 0.1 dpa – which is end-of-life of the first ITER divertor – the samples become active and require hot cell testing as well as fully remote operation, which unfortunately limits a number of experimental techniques to perform post-deformation analysis. In this case, the most common type of testing comprises mechanical and scanning electron microscopy analysis, while application of transmission electron microscopy requires some cooling to enable the sample preparation (conventional or by focus ion beam).

In the present work, we investigate the effect of neutron irradiation on mechanical properties and microstructure of several tungsten grades recently developed. Neutron irradiation campaign is arranged at three temperatures: 600, 800 and 1000 °C and the neutron fluence is limited to 0.2-0.25 dpa range thus being relevant for the ITER plasma facing components. Four different grades are included in the study, namely: fine-grain tungsten strengthened by W-carbide (W-4wt.% W_2C), fine-grain tungsten strengthened by Zr carbides (W-0.5% ZrC), W alloyed with 10 wt.% chromium and 0.5 wt.% yttrium (W-10Cr-0.5Y) and technologically pure W plate manufactured according to the ITER specification. The selected W-based alloys represent new materials specially developed to combat the problem of high irradiation temperature i.e. embrittlement and recrystallization. The alloying by W_2C and ZrC particles leads to an excessive strength, moreover, the W-0.5ZrC material exhibits reduced DBTT (compared to ITER specification grade) and is available in the form of thick plate (i.e. representing high up-scaling potential). The W-10Cr-0.5Y grade is a lab-scale grade included as the material offering the self-passivation protection against the high temperature oxidation, while being fabricated at high temperature (hence, high potential for the recrystallization resistance). The final application of these materials is armour for the plasma facing components, and through this study two questions are addressed: (i) is there any grain growth as a result of the high temperature irradiation; (ii) is there any loss of the fracture strength as a result of the irradiation.

The main reasons behind the selection of the irradiation temperatures are related to the irradiation effects and accumulation of irradiation damage, which are well known to depend on the temperature [38]. In general, the tested materials are suited for the application in temperature range

of the PFC, which is why the resistance against recrystallization is one of the important elements in the design of these materials. The three different temperatures were selected to reflect the operation of W (in the monoblock at a heat load of 10 MW/m^2, see assessment in [39, 40]) above the cooling pipe (600 °C), in the middle of the monoblock (800 °C) and close to the top surface (1000 °C) In addition, from the earlier studies it is known that the accumulation of damage in W at 600, 800 and 1000 °C differs. In particular, at 600 °C at moderate doses, dislocation loops and voids are observed, while at 800-1000 °C, in addition to the voids, Re-Os precipitates are formed thanks to the long-range diffusion [41]. Moreover, a recent direct experimental evidence of the irradiation-enhanced recrystallization in W occurring already at 850 °C and 0.44 dpa is reported in [42], which also drove the selection of the irradiation temperatures for this study.

After the neutron irradiation the bend tests are performed at elevated temperature (up to 600 °C) to assess the mechanical strength and associated fracture mechanisms in the operationally-wise low temperature regime, where the fracture strength is an important material property for structural integrity of the component.

2. Materials, irradiation and testing methodology

For different types of tungsten grades are investigated in this study. As a reference, so-called baseline material, commercial ITER-specification pure tungsten grade produced by Plansee, Austria is used. This material has been already used in a number of studies addressing the plasma-wall interaction [43], annealing and recrystallization behaviour [18] and effect of neutron irradiation [44-46]. We adopt the same label for this material as in the cited above works, which is W-IGP. This material is produced by powder metallurgy and has carrot-like grains because it is hammered into a rod with a 35 mm x 35 mm cross section, more information on the microstructure is presented further. In this work, we refer to this material as "reference" or rather "baseline" material because its production route is considered to be the main option for the supply of PFC components for ITER facility.

The second grade considered is also produced by the powder metallurgy coupled with chemical alloying and thermo-mechanical treatment. By dedicated alloying with zirconium-carbon (ZrC) nano-sized particles and rolling, it was possible to reduce the free oxygen occupying grain boundaries and induce high density of dislocation defects simultaneously (in-depth information about the fabrication, thermo-mechanical treatment and resulting microstructure is provided in [47-49]). Preliminary mechanical and high heat flux (HHF) assessment demonstrated that W-0.5wt.%ZrC alloy exhibits the DBTT around 100 °C and successfully withstand HHF loads up to the power density of 0.66 GW/m^2 [47], simulated by electron beam. The final product is a rolled plate of 12 mm thickness. Given the applied rolling, the material exhibits grain texture. We shall refer to this material as W-ZrC.

The third material is the composite based on the particle-strengthening principle with W$_2$C precipitates. Tungsten powder with an average grain size of 1.5 μm (Global Tungsten & Powders spol. S r.o., Czech Republic) was used in this study. According to the producer's specification, the oxygen content in the powder was 0.105 wt %., i.e., 1.2 at. %. The tungsten powder was mixed with WC powder (150–200 nm, >99%, Aldrich, Germany) in cyclo- hexane (Sigma Aldrich, Germany) and homogenised with an ultrasonic processor VCX500 (Sonics & Materials Inc., USA) for 3 min at a power of 250 W, frequency 20 kHz and pulse on/off of 1 s. The powder mixtures was sintered in a graphite die with an inner diameter of 16 mm using field-assisted sintering (FAST, Dr. Sinter FAST 515-S, Sumimoto FAST Syntex Ltd., Japan) at 1900 °C with a heating rate of 100 °C/min, for 5 min and an

applied pressure of 60 MPa. Before the FAST processing, the reaction chamber was purged several times with high-purity argon and evacuated again. During sintering, the pressure inside the chamber was below 10 Pa. [23]. The added WC completely transforms to W_2C, resulting in a W-W_2C composite. The microstructure, grain size and thermo-mechanical properties of as-produced W-$4W_2C$ is described in section 3.1.3 W-WC.

The forth material is an alloy of composition W-10Cr-0.5Y in wt.% prepared from elemental powders of W (99.95%, 20 μm), Cr (99.95%, 50-70 μm) and Y (99.9%, 20–30 μm) which are mechanically alloyed (MA) under Ar atmosphere in a planetary ball mill using WC grinding jars and balls [50]. After MA, a single (αW,Cr) nanocrystalline supersaturated phase is achieved. Besides, elemental Y is expected to combine with practically all residual oxygen introduced during the MA process, forming Y_2O_3 and cleaning the grain boundaries (GB) from oxygen. The alloyed powder is introduced in metallic capsules, which are evacuated, degassed, sealed and HIPed at 1250 °C for 2 h at 150 MPa [50]. After HIPing, a homogeneous, ultrafine grained microstructure is obtained with an average grain size of the equiaxed matrix below 100 nm. It consists of two main BCC phases, a W rich (αW,Cr) phase and a Cr-rich (αCr,W) one, formed by nucleation and growth, with composition according to the W-Cr phase diagram [51], and an Y_2O_3 nanoparticle (NP) dispersion, located at the GBs, contributing to inhibit grain growth and reinforce the material. The relative density of the resulting as-HIPed material is > 99 %. The presence of two phases with quite different thermo-physical properties is detrimental in view of possible misfit strains and thermal stresses induced by the second phase. Thus, a heat treatment (HT) at 1555 °C under H_2 atmosphere is performed after HIP to obtain a single BCC phase material without the Cr-rich phase. The relative density after the HT is usually above 98%. However, the samples tested in the present work presented a quite lower relative density of about 95%. At the time of sample preparation (given that the irradiation campaign has been launched in 2019), the fabrication process was not yet completely optimized and the powder contained unalloyed Cr particles generating porosity during the phase transition due to the Kirkendall effect connected to the much higher amount of vacancies and higher mobility of Cr atoms compared to W atoms [52]. Nevertheless, the unalloyed Cr particles were found to be homogenously distributed throughout the sample and thus, the pores were homogeneously distributed as well. However, the lower density of the supplied samples results in a slightly lower strength compared to samples with the usual density. The HTed, dense W-10Cr-0.5Y alloy has withstand 1000 thermal cycle loads of 0.38 GW/m^2 power density and 1 ms duration with the appearance of a crack network while the addition of 0.5 wt% Zr to this alloy results in no damage after the same loading [53].

To execute the irradiation, the miniaturized bend bar specimens (1×1×12mm) were loaded in the Belgian Reactor (BR2) in the cycle 2 and cycle 3 of 2019. The specimens were placed inside 1.5 mm-thick stainless steel capsules filled with an inert gas (helium) to prevent the oxidation of the samples during high temperature irradiation. The thick-wall stainless steel capsule acted as a shield to avoid extensive transmutation into rhenium. The typical transmutation rate was ~2 at.%Re/dpa. The samples were fixed inside tungsten holders which were used to achieve 1000, 800 °C and 600 °C irradiation temperature. The temperature was achieved by the balance of the irradiation-induced heat release inside the samples and holders, and heat evacuation through the gas gap to the capsule wall and to the coolant body of the BR2 reactor. Such design has been already applied in a number of recent experiments carried out on tungsten and tungsten alloys, more details are available in [54-56], while

below we provide a brief description of the irradiation experiment. The capsules are embedded inside the fuel element, where the fast neutron flux is in the range 1-5 x 10^{14} n/cm^2/s (En > 0.1 MeV) at a nominal reactor power of 60 MW. The calculation of the irradiation dose in displacement per atom (dpa) units is performed by MCNPX 2.7.0 code [57] using the threshold displacement energy of 55 eV. The irradiation doses and temperatures on the samples are found to be 0.19 dpa (2.48E+20 n/cm^2, E>1 MeV) at 400 °C (capsule TB4E), 0.20 dpa (3.06E+20 n/cm^2, E>1 MeV) at 800 °C (capsule TB5E), and 0.26 dpa (3.44E+20 n/cm^2, En>1 MeV) at 1000 °C (capsule TB6E) using the MCNP calculations (neutron flux, gamma flux, heat release due to prompt and delayed gamma and neutron heating), reactor power measurements, and finite element thermal calculations (the irradiation temperatures are nominal values calculated as average during the cycle). During the reactor cycle, the actual temperature on the samples exhibits an excursion of about ±15% with respect to the nominal value. The ALEPH code of SCK CEN [58] and accessible nuclear databases [59-61] are applied for the calculation of transmuted elements. It should be noted that the presence of carbon in two grades (W-0.5ZrC and W-4(W$_2$C)) would promote the formation of He in DEMO spectrum from ~0.5 appm for pure tungsten to 3.65 appm for W-0.5ZrC alloy at 1 dpa. However, in the BR2 mixed spectrum, the effect of carbon in terms of the formation of He is negligible.

Miniaturized bending specimens were tested according to ASTM E290 standard using the three-point bending (3PB) stage installed inside the environmental furnace. The span between the lower supporting pins is equal to 8.5 mm and their diameter is 2.5 mm. The samples had dimensions 1×1×12 mm^3 with a mirror-like surface. Given the technological importance, T-L orientation has been used for the materials with texture (W-IGP). The T-L orientation, as defined in the ASTM standard E399, corresponds to the situation when the crack propagates along the elongated grains, while the long axis of the sample is oriented along transversal direction. The tests were performed on a universal testing machine Instron equipped with a furnace operated in air, which is why the uppermost temperature was set to 600 °C. The test temperature was measured by a thermocouple located close to the specimen. The load and displacement were measured with a strain gauge based load cell and a position encoder for the actuator, respectively. A constant displacement rate of 0.723 mm·min^{-1} was applied, equivalent to the (flexural) strain rate of 10^{-3}·s^{-1} along the stretching side of the specimen.

The flexural strain (FS) is determined as:

$$FS = \frac{6Dd}{L^2} \qquad (1)$$

where D is the maximum deflection of the specimen, d is the sample thickness, and L is the span between the lower pins. The flexural strain is accordingly calculated using the pull rod displacement and linear slope method to characterize the amount of plastic strain. The determination of the flexural strain (elastic and plastic) is done by the decomposition of the load-displacement curve into elastic and plastic parts, full details of such tests are provided in Ref. [62]. For the neutron irradiated samples, at least two tests per test temperature are executed.

To provide a primary information on the fracture mechanisms after the neutron irradiation, scanning electron microscopy (SEM) was applied. The surface imaging was performed using SEM JEOL 6610 with secondary electron detector (accelerating voltage 15 kV and working distance of 10^{-11} mm) inside the hot cells enabling investigation of the irradiated samples. Electron back scattering diffraction (EBSD) and EDS chemical analysis could have been performed only in the non-irradiated state due to the relatively high residual activity on some samples (exceeding 20 mSv/hour on contact even 2 years after

the irradiation). The excessive gamma irradiation is detrimental for the operation of the EBSD and EDS detectors.

3. Results and discussion

The results are presented in three sub-sections reporting reference measurements, results of mechanical tests after the irradiation and fracture surface after the irradiation. When presenting the result of the bending strength we also provide trend curves to "guide an eye". SEM images are supplied with marks and arrows to refer to specific microstructure discussed.

3.1 Microstructure and Mechanical properties of materials in non-irradiated state

Each of the studied grades has been inspected in terms of the microstructure and bending performance as a function test temperature. In the case of the advanced grades (W-WC and W-10Cr-0.5Y), the detailed inspection was carried out in parallel with neutron irradiation. The primary tests on the non-irradiated samples were performed by the labs supplying the materials, however, the reference bending tests at RT, 300 and 500 °C were also performed at SCK CEN using the same equipment as applied to test as-irradiated samples. The bending tests and SEM analysis of the fracture surface after the irradiation were performed at SCK CEN in the hot cells.

The most important information in terms of the mechanical performance is the DBTT and bending strength. At this, depending on the deformation/fracture mode, it is relevant to repot either the strength at fracture (for the brittle mode) or an apparent yield point (in the ductile mode leading to the bending of the sample without fracture), as the latter value can be directly correlated with the tensile strength otherwise extracted from the uniaxial tensile test [62]. In the following, we shall use a generic term "bending strength" while referring either to the fracture or yield bending stress depending on the deformation mode.

Bending strain to fracture is another important value which can be used to deduce the DBTT range, as was shown on the example of W-IGP [63]. The DBTT has been extracted using the 5% bending strain criterion [64]. For the studied materials, the DBTT was determined to be 140-160 °C for W-ZrC, 380-400 °C for W-IGP (T-orientation), 600-800 °C for W-WC and 1000-1100 °C for W-10Cr-0.5Y (for the material with > 98% relative density). The range for the determination of the DBTT depends, among others, on the density (on temperature scale) of the test points, which was relatively low for the W-WC and W-10Cr-0.5Y grades. The relatively high DBTT of these grades is not surprising given that no mechanical treatment (e.g. rolling, forging) was applied to reduce the DBTT (even though in the case of the W-Cr-Y alloy it is questionable whether the DBTT can be reduced due to the high amount of Cr dissolved in the W lattice[1]). In the following, it will be shown that those grades exhibit a porosity which may provide an extra contribution to the DBTT. Yet, as was discussed in the introduction, the primary requirements imposed to those grades in terms of the mechanical properties were the high strength and resistance against recrystallization.

Fig.1 presents the comparison of the bending strength as a function temperature. Correspondingly, the values for each performed test are reported, namely: $\sigma_{0.2}$ – flexural bending stress at 0.2% of the bending strain or σ_f – flexural bending stress at fracture. We can indeed see that the advanced grades

---

[1] E. M. Savitskii and G. S. Burkhanov, Physical metallurgy of refractor y metals and alloys, Consultants Bureau, New York-London, 1970 pg. 199

exhibit higher bending strength as compared to W-IGP in the low temperature range, up to ~400 °C. The strength of W-ZrC and W-WC grades exceed the one of the W-IGP in the whole temperature range studied. The strength of the W-10Cr-0.5Y grade becomes comparable or even lower than that of W-IGP above 1000 °C.

The strength and ductility are naturally determined by the microstructure of the materials, hence in the following sub-sections we describe the microstructure of each tested grade. We also present the fracture surface of the samples tested in the vicinity of the DBTT to link it with the fracture mechanisms occurring around DBTT.
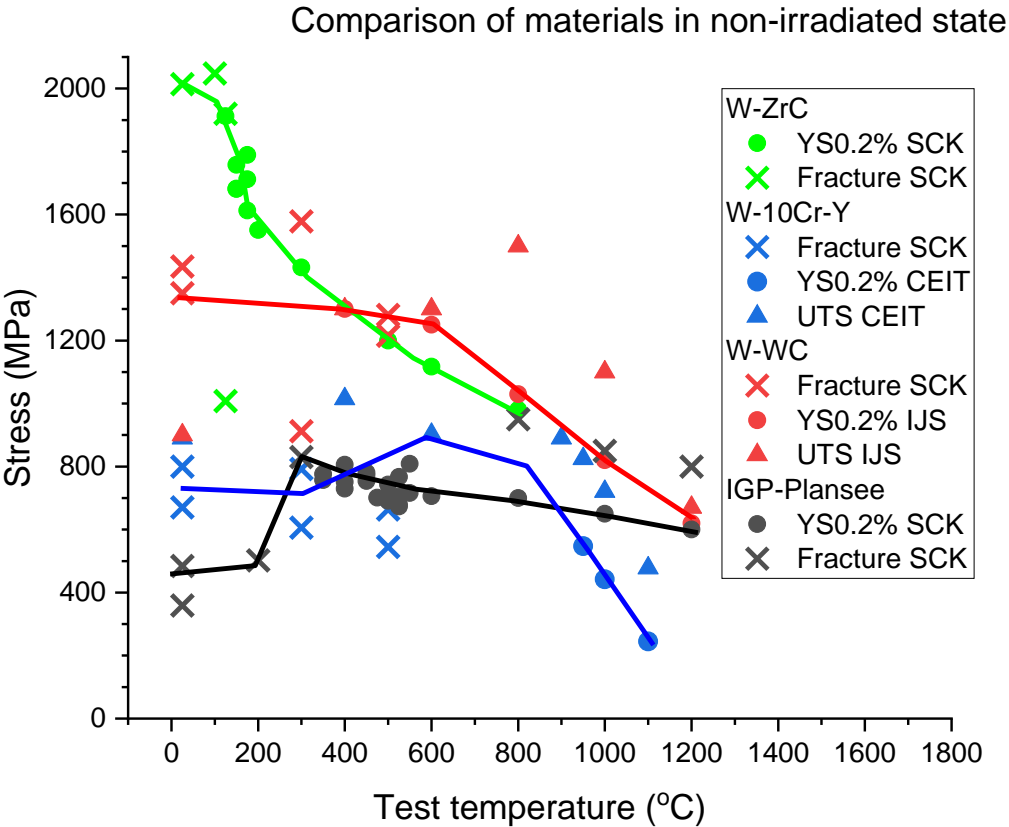
Fig.1. Comparison of the bending strength of different tungsten grades. Three different stresses are reported: YS0.2% is the flexural stress at 0.2% flexural bending stain, UTS is the maximum flexural strain registered during the test in the case of ductile deformation, and Fracture stress in the case of the brittle deformation.
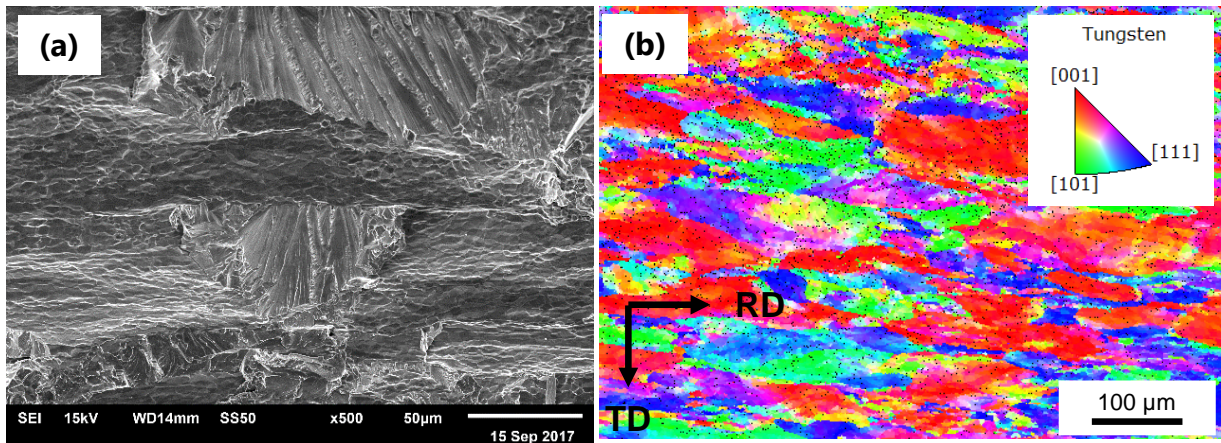
3.1.1 W-IGP

Fig.2. (a) SEM image of the fracture surface of the W-IGP sample tested at 400 °C in the T-L orientation. (b) SEM-EBSD scan, normal direction is perpendicular to the view. RD and TD refer to the rolling and transversal directions, respectively.

As noted above, the W-IGP is the forged bar of 99.97% purity which was produced according to the ITER specification in a form of squared cross section bar (see more information in [43]). The bar was fabricated by hammering on both sides. The grains are therefore needle-like and are elongated along the bar axis. The elongated grains can be well seen on the SEM image of the fracture surface of the T-L bend sample tested at 400C, given in Fig.2a. The fracture near the DBTT consists of two patterns: (i) intergranular and (ii) transgranular cleavage, both appearing in nearly equivalent proportions.

The EBSD analysis (see Fig.2b) revealed that grains with high misorientation angle (> 15 degrees) are elongated with a size of 5-20 μm and 10-100 μm, normal and along to the bar axis, respectively. The presence and morphology of sub-grains was studied by TEM, as EBSD has too low resolution for that purpose. TEM measurements revealed sub-grains are also elongated and their size varies in the range 0.6 – 1.7 μm and 2.3 – 4 μm, respectively, normal to and along the elongation directions. The material does not contain any precipitates [65].
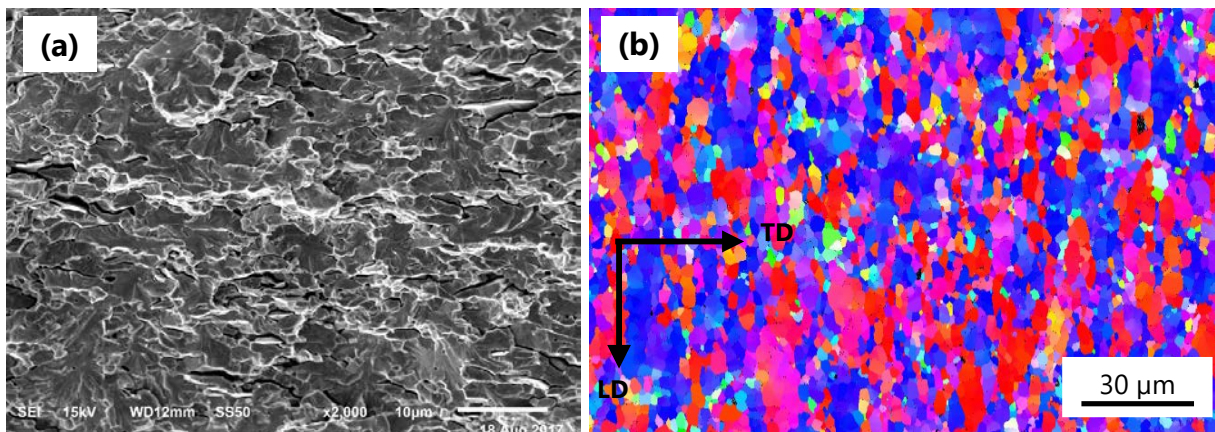
3.1.2 W-ZrC

Fig.3. (a) SEM image of the fracture surface of the W-ZrC sample tested at 160 °C in the T-L orientation. (b) SEM-EBSD scan of W-ZrC grade, normal direction is perpendicular to the view. RD and TD refer to the rolling and transversal directions, respectively.

W-ZrC is a hot rolled tungsten plate of 8 mm thickness reinforced with 0.5 wt% of ZrC produced by the Institute of Solid State Physics, Chinese Academy of Science. As discussed above, the DBTT of this material is around 160-200 °C. The SEM image of the fracture surface of the sample tested at 160 °C is presented in Fig.3a. One can clearly see the intergranular fracture with the presence of lateral micro-cracks implying the delamination of the grains and micro-cracks deflection prior the fracture. Very few regions with the transgranular cleavage are also present. The medium grain size of this material is ~7 μm, as determined by the analysis of the SEM-EBSD scan (see Fig.3b) [66]. The rolling was applied after the sintering, and W-ZrC was processed following a thermo-mechanical treatment to reduce grain size and have nearly equiaxed grains [66, 67], which is why there is only minor difference of the mechanical properties and microstructure between T- and L-orientation. The microstructure of the W-ZrC material exhibits high density of small ZrC particles. The particles are roughly spherical in shape and their size is in the range 100-200 nm. Rarely, particles with a size up to 0.5 μm are observed. The particles are located inside the grains and at grain boundaries. Many particles are interconnected with each other by grain boundary interfaces thus forming a sort of honeycomb network, which is also consistent with the SEM-EBSD images (if seen at high magnification).

Detailed analysis of the microstructure of the W-IGP and W-ZrC grades in the non-irradiated state is provided in [68], where grain size, texture and dislocation density were assessed by SEM and TEM.

3.1.3 W-WC

Microstructural analysis of as-sintered $W-4W_2C$ samples reveals isotropic nature of grains present in the sample. The EBSD studies presented in [23] showed that the W_2C grains are mainly positioned at W grain boundaries, preferentially at triple junctions. The grain size analysis showed that the mean W_2C grain size is approximately 1 μm, while for the W grains is 7.5 μm in diameter. Fig.4a represents SEM micrograph of a fracture surface of $W-4W_2C$ before neutron irradiation. It can be seen that intergranular fracture is dominant, with some scattered transgranular cleavage also present. Some intergranular and grain boundary porosity can be observed, too. The SEM-EBSD scan of the grain pattern is shown in Fig.4. Following the EBSD analysis the median grain size was determined to be 3.8 μm. Mechanical characterization [23] from RT to 1000 °C has revealed that the sample $W-4W_2C$ displayed the highest ultimate flexural strength at 400 and 600 °C. The DBTT was also in this range. W_2C inclusions are ceramic material, which causes an increase in the DBTT of metallic W. Measurements of thermal conductivity (TC) up to 1000 °C revealed that W_2C inclusions slightly decrease the TC when compared to the pure tungsten, which is ascribed to the low TC of the W_2C. The sample $W-4W_2C$ exhibits 120 W/m.K at room temperature, while at 1000 °C the value does not drop below 100 W/m.K [23].
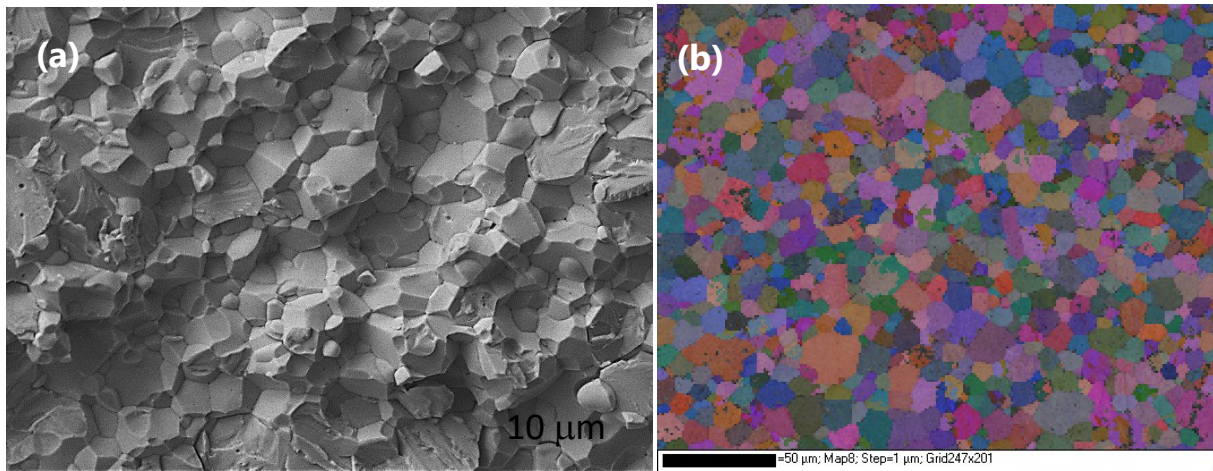
Fig.4. (a) SEM fracture surface of a W-WC sample. (b) SEM-EBSD scan of W-WC sample.
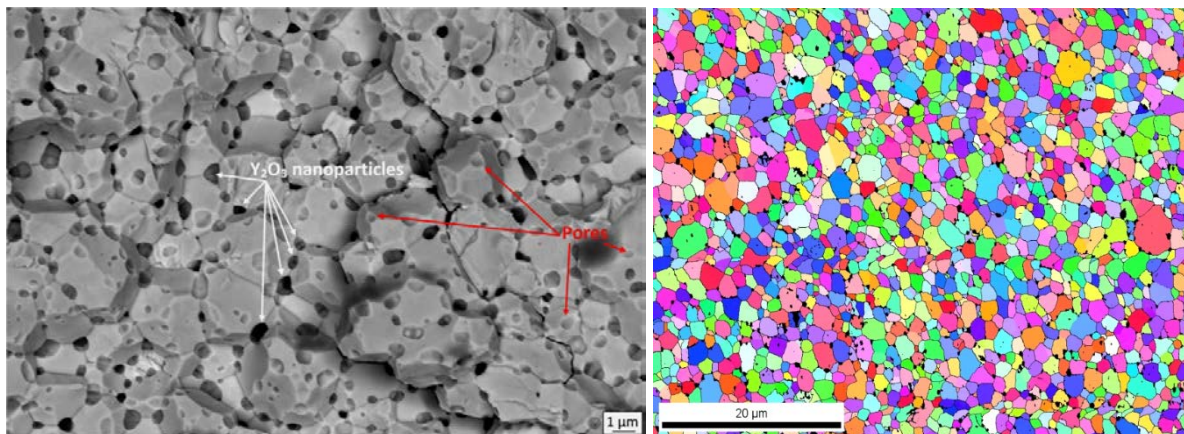
3.1.4 W-10Cr-Y

Fig.5. (a) SEM fracture surface of a W-10Cr-0.5Y sample. (b) SEM-EBSD scan of W-10Cr-0.5Y sample (without porosity)

The fracture surface of the W-10Cr-0.5Y alloy measured at 25°C is shown in Fig. 5a while in Fig. 5b a SEM-EBSD scan corresponding to a sample produced with the same manufacturing parameters but without porosity is presented. The microstructure consists of a metastable single BCC (αW,Cr) phase with equiaxed grains of average size 770 nm. The dark grey minority phase, located mainly at the GBs, corresponds to the Y_2O_3 nanoparticles, as indicated by white arrows in Fig.5a, exhibiting an average size of ~50 nm. As mentioned above, the samples used in the present work have a porosity of about 5 %, which is homogeneously distributed throughout the sample. Pores are mainly located at the GBs and triple junctions, as indicated by red arrows in Fig. 5a. The pores have a size lower than ~ 60 nm in most of the cases. At 25 °C the fracture is mainly intergranular with isolated transgranular cleavage; no defects are visible inside the grains. At 500 °C intergranular fracture is dominant. The flexural strength of the material without porosity has been measured in the temperature range 25 to 1100 °C

[30]. The material has a DBTT of ~950 °C with ultimate flexural strength in the range 900-1000 MPa. The alloy exhibits a thermal conductivity of 51 – 53 W/(m·K) in the temperature range 400 – 600 °C.

Neutron irradiation tests were performed at irradiation temperatures of 600, 800 and 1000 °C for 50 days. Since the W-10Cr-0.5Y alloy after HT presents a metastable microstructure, samples were exposed in a previous work [50] to a temperature of 650 °C for 3000 h to study the thermal stability of the microstructure under operational conditions. After the ageing test, there were no significant changes, as the microstructure of the material as well as its density and hardness remain unchanged (Fig. 6c). Therefore, it is expected that no major microstructural changes will be observed after irradiation test at 600 °C unless those produced by irradiation damage. After 100 h at 800 °C, only slight grain growth was observed. However, at higher magnification, the onset of the phase decomposition at the GBs in form of lamellae of Cr-rich and W-rich phases was observed (Fig. 6b). The mechanism for the formation of such a lamellar structure is associated with the spinodal decomposition. The miscibility gap of W-Cr phase diagram is represented next to the chemical spinodal line (blue dashed line) in Fig. 6. Within the miscibility gap, the formation of two different phases is expected. However, the formation mechanisms of these phases depend on the position in the phase diagram (chemical composition and temperature) with respect to the chemical spinodal line. This line represents the inflexion points of the isothermal free energy (G) – composition curves, i.e. the points where $\frac{\partial^2 G}{\partial C^2} = 0$. Therefore, within the chemical spinodal line where $\frac{\partial^2 G}{\partial C^2} < 0$, the single-phase is unstable and spinodal decomposition takes place. In this case, the phase formation should be only produced by atomic diffusion processes. Outside the spinodal area, the phase is metastable where G can only be reduced by nuclei formation, i.e. the two phases should be formed by nucleation and growth. As can be observed in Figure 6, the selected irradiation temperatures are within the chemical spinodal region. Thus, a microstructure composed of Cr-rich and W-rich lamellae should be obtained. However, at 600 and 800 °C, the temperature is too low for activating diffusion processes, especially for W. Therefore, very long times would be required for the microstructure to achieve the decomposition. For this reason, no significant changes in the microstructure are expected after irradiation up to 800 °C. The fact that in our system the decomposition starts at the GBs indicates that nucleation and growth is taking place, probably because of the effect of the strain energy produced by the mismatch between the atomic sizes of Cr and W, as stated by Porter [69].

Figure 6. Miscibility gap of the W-Cr phase diagram with the chemical spinodal boundary indicated by the blue dashed line calculated using the Thermo-Calc software. Microstructures obtained after ageing at the temperatures of the irradiation tests are indicated.

After ageing at 1000 °C for 50 and 100 h, the microstructure exhibits a phase decomposition with significant grain refinement (Fig. 6a). After 50 h, the Cr-rich phase presents a lamellar shape while after 100 h, a vermicular shape typical for spinodal decomposition has been developed [50]. Based on these results, a complete phase decomposition with vermicular microstructure and large grain refinement is predicted after the irradiation test of W-10Cr-0.5Y samples annealed at 1000 °C lasting for more than 50 days. Such a transformation leading to uniform, fine-scale, two-phase mixture can significantly enhance the mechanical properties of alloys presenting spinodal decomposition, as reported in the literature [70].

3.2 Mechanical properties in as-irradiated state

The mechanical tests presented and discussed in this section cover the test temperature range of RT-600 °C. This range is due to the capability of the hot cell equipment currently limited to the maximum test temperature of 600 °C. To avoid intensive oxidation of tungsten, we limited the uppermost test temperature to 500 °C. This is why the mechanical properties will be delivered at two limiting temperatures being RT and 500 °C, and at the intermediate temperature chosen to be 300 °C.

The bend strength of W-IGP before and after irradiation is presented in Fig.7. At the maximum test temperature covered in this study (500 °C), all tested samples appear purely brittle fracture implying that the DBTT exceeds 500 °C. Hence, the DBTT shift is above 100 °C, which is consistent with the DBTT shift of 100-150 °C obtained for the same material (but for L-orientation) irradiated at 400 and 800 °C

13

at 0.15-0.2 dpa [44]. One can also see that the fracture stress for T_{irr}=800 and 1000 °C increases as the test temperature increases from 300 up to 500 °C. This can be interpreted as a contribution of the thermally activated plastic deformation at the micro-scale, meaning that 500 °C could be close to the DBTT value. Irrespective of the suppression of the macroscopic plastic deformation, the fracture strength of the irradiated samples does not drop below 400 MPa which is the value established for the non-irradiated samples in the brittle mode. Hence, the irradiation does not cause the reduction of the fracture stress in the brittle regime for this grade.

The bend tests executed on the W-ZrC, see Fig.8, have revealed the brittle behavior at T_{test}=RT (as expected), semi-ductile behavior at T_{test}=300 °C and ductile deformation at T_{test}=500 °C. Given this observation, some extra tests were performed in the vicinity of 300 °C to define better the DBTT.

The fracture flexural strain increases from zero to above 10% within rather narrow temperature interval (50-100 °C), the maximum flexural strain can serve as a good indicator for the identification of the DBTT region. Earlier, it has been already shown that it provides rather good correlation with the DBTT region defined from the conventional fracture toughness tests [71]. Thus, the DBTT of W-ZrC after the irradiation was determined by fitting the strain at fracture and setting up a threshold above which the material could be considered as ductile. The upper threshold of the flexural strain (FS_{top}) is defined as 10%, and the lower base of the flexural strain (FS_{base}) is defined as 0%, and the equation to fit the transition curve reads:

$$FS(T) = \frac{10\%}{1+exp\big(C(T_{half}-T)\big)}$$

(2)

where C is the slope of the transition curve; T is the test temperature. T_{half}, which is also defined as the DBTT after the irradiation (following the 5% criterion proposed in Ref. [72]), is the temperature corresponding to flexural strain equal to 5%. Note that we refer to 5% of plastic flexural strain, which is calculated by subtracting the elastic strain from the load-displacement curve.

The bending stress-strain curves obtained at 300 °C are presented in Fig.8a. One can clearly see that the bending strain at fracture is much lower for the samples irradiated at 1000 °C. Another interesting feature is the evolution of the bending stress after the yield point, which also depends on the irradiation temperature. At T_{irr}=1000 °C, the bend stress logarithmically increases up to the fracture point in a similar way as it happens in the non-irradiated sample, while for the lower irradiation temperatures the bending stress exhibits the linear reduction as soon as the yield point is reached. The behavior could be attributed to the different nature (i.e. loops/voids/Re-Os precipitates) as well as to the difference in density of the irradiation defects formed at high and low irradiation temperature.

The strain to fracture as a function of temperature is presented in Fig.8b. Applying these results and Eq.(2), the DBTT after the irradiation at T_{irr}=600 and 800 °C was determined to be 330 °C (DBTT shift is 190 °C). The fracture strain of the samples irradiated at 1000 °C was less than 5% and therefore the DBTT exceeds 500 °C. These results also demonstrate that 1000 °C irradiation causes a larger DBTT shift in W-ZrC i.e. higher irradiation temperature causes more severe damage, which is not obvious result.

The bend strength of W-ZrC before and after the irradiation is presented in Fig.9. The results reveal two important observations: (i) there is a significant reduction of the bend strength at RT (i.e. in the brittle mode) after the irradiation; (ii) the bending strength near DBTT is comparable before and after

the irradiation. The first observation implies that the fracture stress in brittle deformation regime is decreased by the neutron irradiation, irrespectively of the applied irradiation temperature. Hence, some microstructure which ensured high strength in the brittle mode before the irradiation is apparently removed (or becomes not active) after the irradiation. TEM investigation would be needed to clarify the reasons for this effect.

The bend strength of W-WC before and after irradiation is presented in Fig.10. The results show that the room temperature bend strength depends on the irradiation temperature. In particular, the strength is reduced below the reference value for the irradiation temperature of 800 and 1000 °C. Tests at 300 and 500 °C reveal that the fracture stress is essentially increased from about 1200 up to 1600 MPa for all irradiation temperatures. The only exception is noted at T_{irr}=800 °C, at which the fracture stress remains below the reference value at T_{test}=300 °C. Given that the DBTT of this material was already in the range of 400-600 °C, the carried tests could not reveal the DBTT shift and all test returned fully brittle fracture (as was expected). The main observation resembles the loss of strength at RT, and increase of the strength at elevated temperature.

The bending strength of W-10Cr-0.5Y before and after the irradiation is presented in Fig.11. As in the case of W-WC, the W-10Cr-0.5Y grade exhibits DBTT above 500 °C and therefore the DBTT shift could not be revealed with the present set of tests. In Fig.11 the bending strength of the material without porosity is also shown to demonstrate the effect of porosity on the reduction of the strength in non-irradiated state. Within the executed test temperature range, the neutron irradiation yielded an increase of the fracture stress. In the case of 1000 °C irradiation, the increase of the fracture stress was especially high (a factor of two to three, depending on the test temperature). The increase of the stress due to 600 and 800 °C was similar and yielded to about 50% of the reference fracture stress. The increase of the fracture stress was registered at all test temperatures.
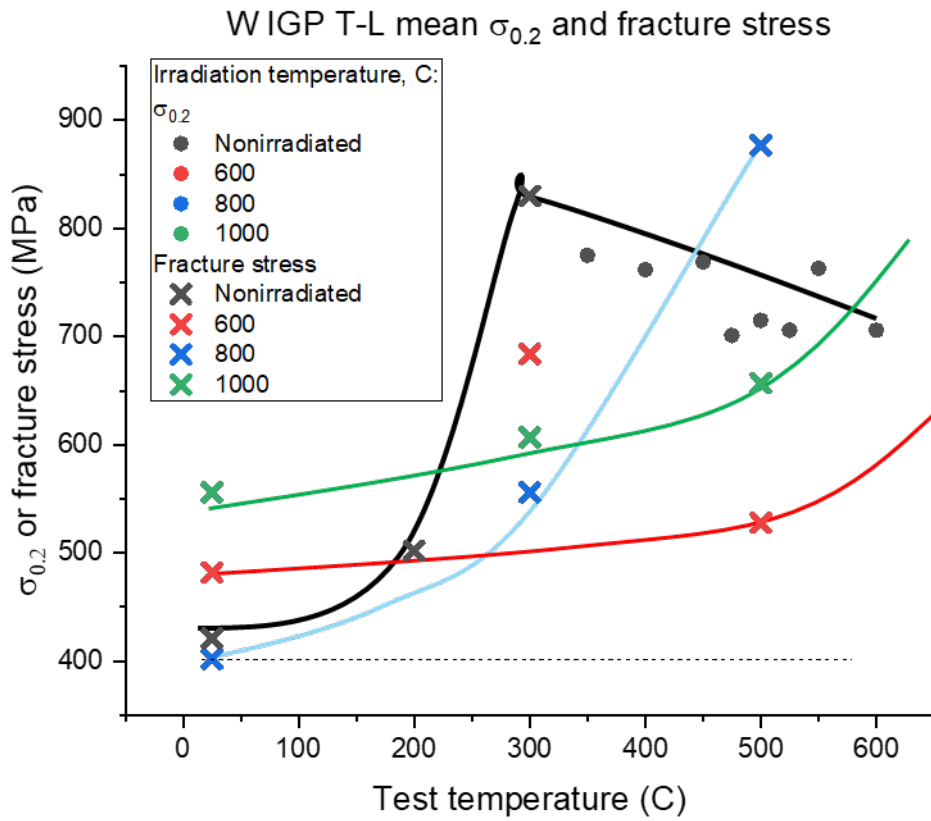
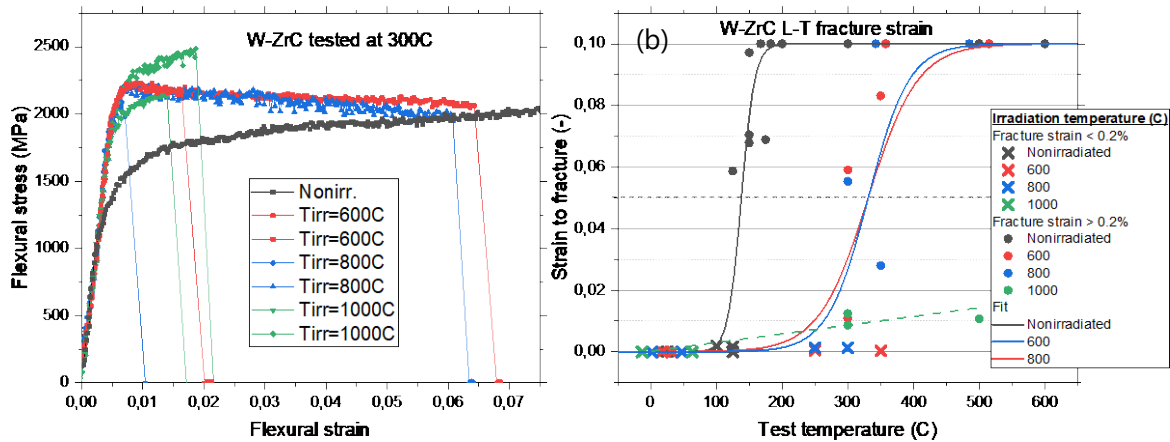Fig.7. Bend strength of W-IGP (T-L orientation) before and after the irradiation.

Fig.8. (a) Flexural stress-strain curves obtained for W-ZrC at T_{test}=300 °C. (b) Strain to fracture as a function of test temperature for W-ZrC.
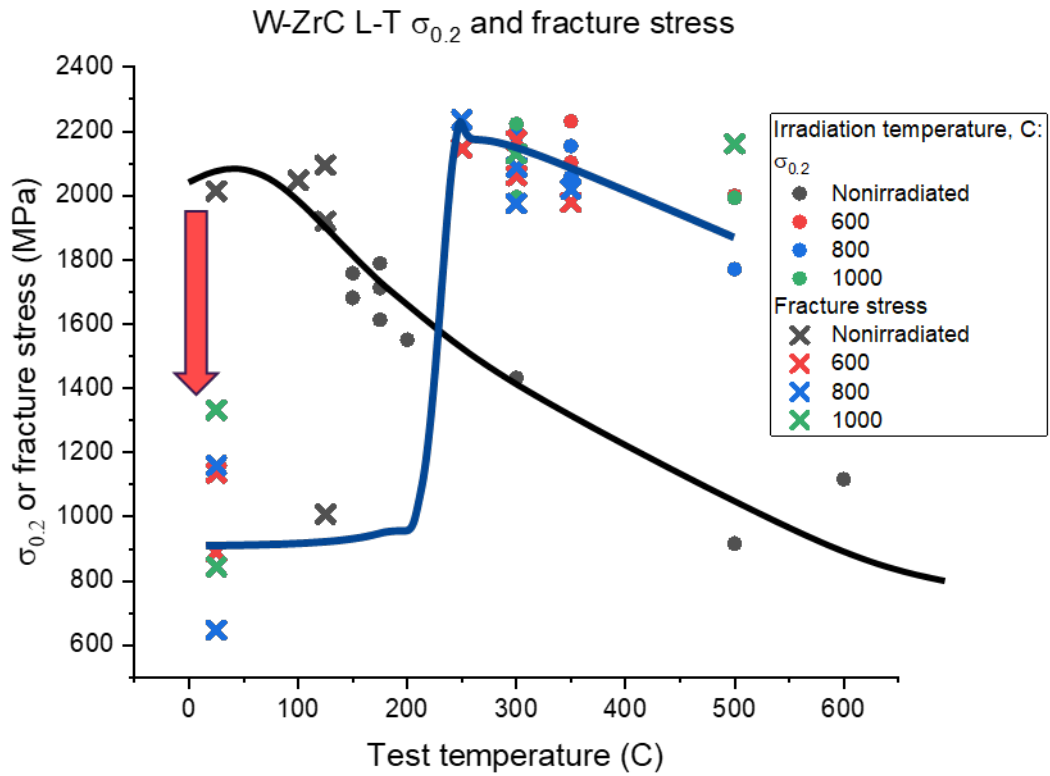
Fig.9. Bend strength of W-ZrC before and after the irradiation. Red arrow points at a pronounced reduction of the fracture stress at RT. Ductile deformation after the irradiation shifts to the temperature range above 300-400 °C, except for the samples irradiated at 1000 °C.
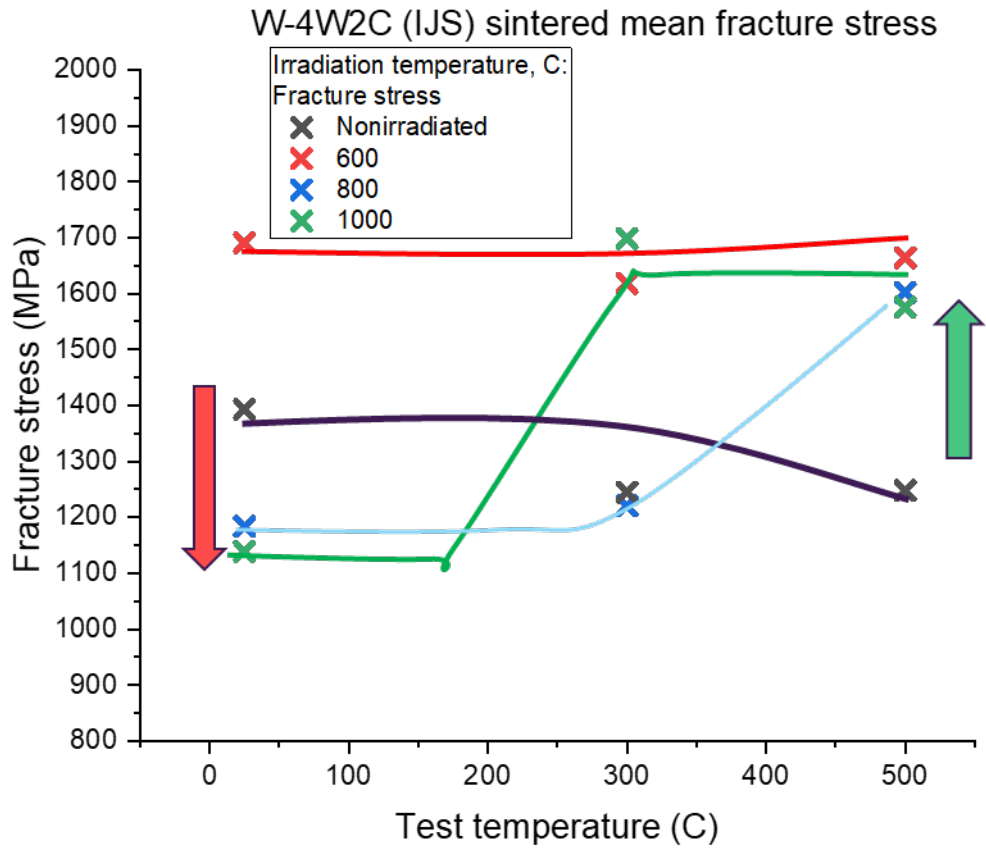
Fig.10. Bend strength of W-WC before and after the irradiation. Red arrow points at the reduction of the fracture stress. Green arrow points at the increase of the fracture stress after the irradiation.
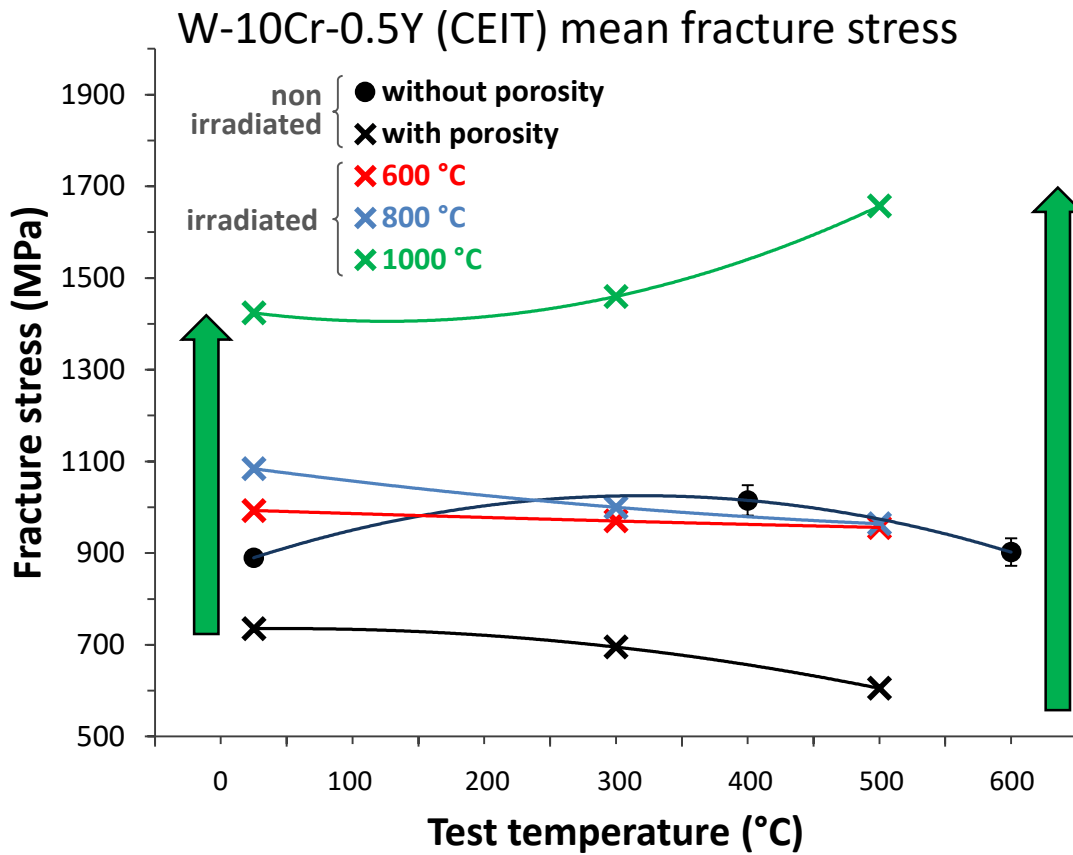
Fig.11. Fracture stress of W-10Cr-0.5Y vs test temperature before and after the irradiation. For comparison, the non-irradiated material without porosity is included, which exhibits a higher strength compared to the one with porosity used in the present work (see section 2). The green arrows point at the increase of the fracture stress after the irradiation.

3.3 Fracture surface analysis after irradiation

The primary purpose of the SEM analysis after the irradiation was to identify whether any essential grain growth took place, since the resistance of the materials against the grain growth was important property to validate. This is why we focus on the SEM images of the samples fractured at room temperature because those correspond to the brittle fracture (for all samples studied) and therefore good appreciation of the pattern of fractured grains could be obtained.

The fracture surface of the W-IGP after the irradiation was very similar to the one presented in Fig.2a, which corresponds to the mixture of the intergranular and transgranular fracture. Although after the irradiation the portion of the transgranular cleavage area has increased making it approximately 70% over all the surface. Judging from the grain pattern that can be seen on the transgranular fracture areas no grain growth occurred at all applied irradiation temperatures. Given that no specific features on the fracture surface of the W-IGP were observed after the irradiation we omit to present SEM images for the sake of conciseness.

The fracture surface images of the W-ZrC samples irradiated at 600 and 1000 °C are presented respectively at Fig.12a and Fig.12b. The irradiation has led to the formation of the large transgranular cleavage areas (only small islands were observed before the irradiation) at both irradiation temperatures. Often, the cleavage ribbons were observed in the transgranular cleavage area. In addition, the presence of a high density of sub-micrometer (0.05-0.1μm) pores was also evident on the transgranular cleavage areas. There were no pores observed on the grain boundaries or at grain triple junction vertices. Given that the dimension of the pores is too large to classify them as voids formed due to the irradiation, those pores could resemble debonded ZrC particles. Apparently, such pores were not observed on the non-irradiated samples because the transgranular cleavage represented only a minor fracture and intergranular fracture was the main mode. The strong increase of the transgranular cleavage fracture is consistent with the reduction of the strength observed in W-ZrC after the irradiation (see Fig.7). Apparently, the irradiation defects suppress sub-grain micro-deformation and the crack deflection via grain boundary surface cannot be sustained so that crack propagates directly through the sub-grains and grains. The regions owing the intergranular fracture were specially inspected to check the size of the grains, and the grain size was found to remain as small as before the irradiation.

The fracture surface images of the W-WC samples tested at room temperature are presented in Fig.13. Before the irradiation, the fracture surface consists mostly of the intergranular fracture (see Fig.4). After the irradiation at 600 °C, the interganular fracture remains to be the dominant mode as shown in Fig.12a. The irradiation at higher temperature yielded in the cracking of the grains i.e. transgranular fracture dominated, see Fig.13b and Fig.13c. This observation is consistent with the fact that the fracture strength was reduced after irradiation at 800 and 1000 °C in the tests carried at RT (see Fig.9). The pores of sub-micrometer sizes were observed in all the samples consistently before and after the irradiation. The irradiation did not result in the appearance of the pores at T_{irr}=600 and 800 °C. While, the density of the observed pores seems to be lower after the irradiation at 1000 °C, the pores are larger in size, especially the pores located at the GB interfaces (or triple junctions) have grown.

However, what appears to be large pores at the grain boundaries (triple junctions) are voids left after the (most likely W_2C) grains were pulled-out during fracture tests. Similar behavior was also observed in the samples (with the same composition) after the ageing at temperatures above 1000 °C [23]. The decrease in the RT strength of the samples irradiated at 800 and 1000 °C is in accordance with the results on the aged samples with the same composition [23] in which the decrease of RT flexural strength was observed too. Presumably, the additional thermal treatment above certain temperature strengthens the grain boundaries (i.e. rectifies the grain boundary interfaces) leading to the crack deflection and transgranular cleavage appearance. By comparing the grain size before and after the irradiation using SEM images of the fracture surface, no increase of grain size could be registered.

The fracture surface images of the W-10Cr-0.5Y samples fractured at room temperature are presented in Fig.14. The fracture surface at 600 and 800 °C was essentially similar, and therefore we provide only the images for T_{irr} = 600 and 1000 °C. The fracture pattern at T_{irr} = 600 °C (see Fig.14a) is quite similar to the one observed before the irradiation near DBTT (see Fig.5). After irradiation at 600 °C, the transgranular cleavage area somewhat increased. Numerous pores appear as seen on the fracture surface before the irradiation (see Fig.5). After irradiation at 1000 °C, the fracture surface is completely different, see Fig.14b. Large cavities are present, inside which a vermicular microstructure typical for spinodal decomposition is visible. The fracture of this microstructure is purely transgranular. As

explained before, a complete spinodal decomposition of the initially single-phase microstructure is expected after more than 50 days irradiation at 1000 °C. This is the microstructure visible inside the cavities of Fig. 14b, which have been formed most probably by coalescence of the initial pores. The spherical sizes of these initial pores located at the GBs and triple junctions indicate that they have reached equilibrium. However, at an irradiation temperature of 1000 °C, diffusion processes are much faster than at 800 °C so that individual pores can merge by GB dragging and grow by GB diffusion of vacancies to larger pores [73]. Besides, phase transformation taking place during 1000 °C irradiation leads to the creation of new GBs, which can promote the coalescence of pores. Moreover, the irradiation dose of 0.26 dpa at 1000 °C can contribute to increase cavities due to the formation of voids, even though this has to be further investigated since there are only scarce data on neutron irradiation of W at 1000 °C [74] while the effect of additional Cr is unknown. The mechanical properties of this spinodal-like microstructure has to be assessed to compare the results obtained in this work with those of an unirradiated material without porosity. In any case, it seems plausible to assert that the formed spinodal-like microstructure is responsible for the strong increase in strength after 1000 °C irradiation at all test temperatures due to the uniform, fine-scale, two-phase mixture in spite of the cavity formation. The size of the cavities observed in Fig. 14b is below ~10 μm. In a material without initial porosity a significantly lower cavity formation or cavity size would be expected since only voids formation by irradiation and their interaction with GBs would contribute to the growth of cavities. The absence of initial pores could contribute to increase the strength to values higher than those obtained in this work after 1000 °C irradiation since pores and cavities act as stress concentrators reducing strength. Taking into account the obtained results, it would be very interesting to produce a W-10Cr-0.5Y alloy in which such a spinodal-like microstructure is promoted and to study its mechanical properties before and after irradiation.

The increase in strength observed at 600 and 800 °C irradiation can be associated to the start of lamellae formation of the two phases at the GBs after long time irradiation. The additional effect of neutron irradiation has to be elucidated.
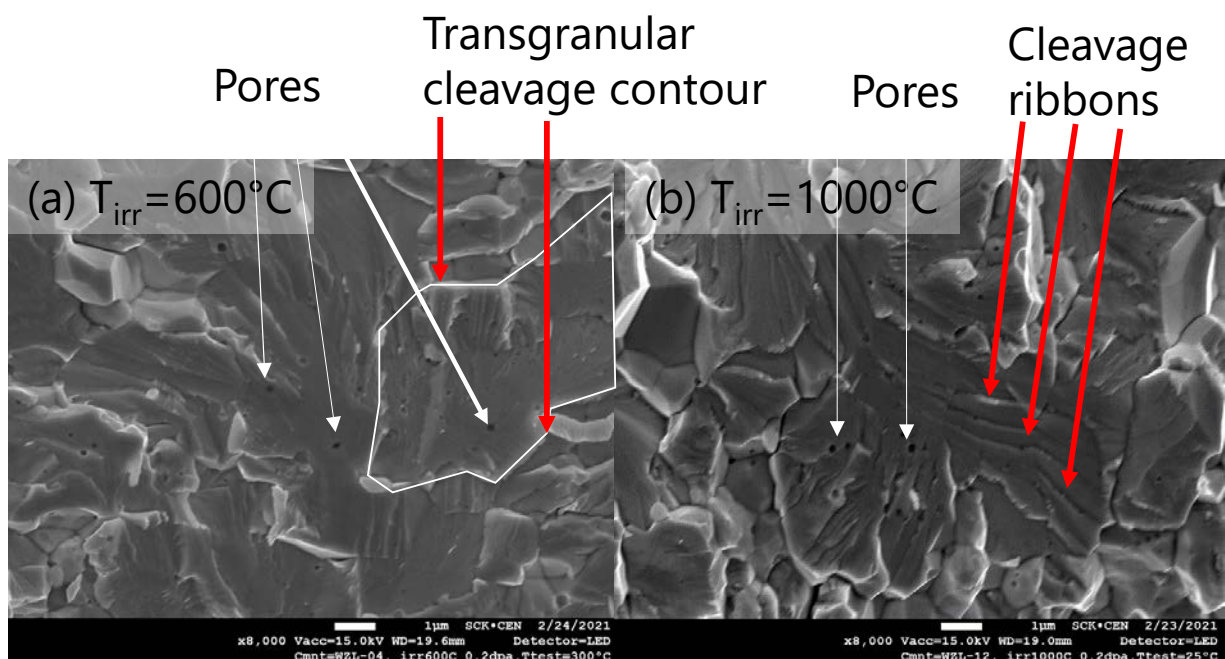
Fig.12. Fracture surface of the W-0.5ZrC sample tested at room temperature. (a) sample irradiated at 600 °C; (b) sample irradiated at 1000 °C.
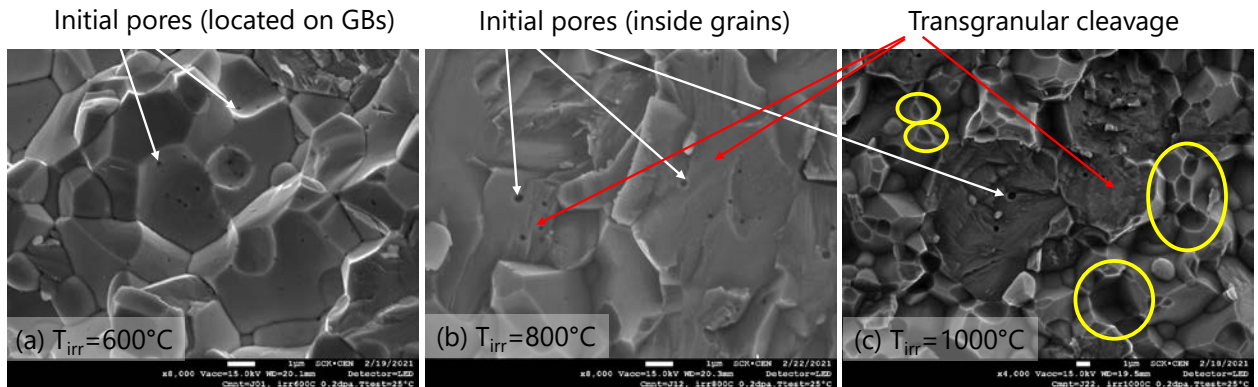

Fig.13. Fracture surface of the W-WC sample tested at room temperature. (a) sample irradiated at 600 °C; (b) sample irradiated at 800 °C; (c) sample irradiated at 1000 °C. Yellow circles on (c) show the pulled-out grains due to the sample fracture. Smaller craters correspond to W_2C grains, larger ones represent tungsten grains.
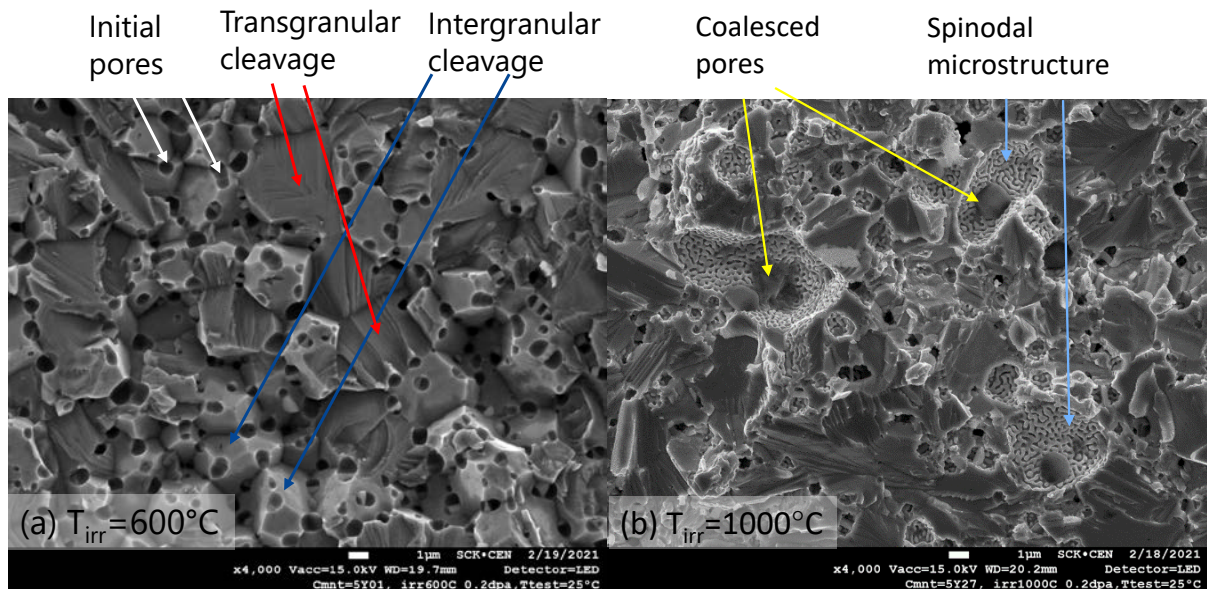

Fig.14. Fracture surface of the W-10Cr-0.5Y sample tested at room temperature. (a) sample irradiated at 600 °C; (b) sample irradiated at 1000 °C.

3.4 Summary of the experimental observations

To summarize, the effect of neutron irradiation on mechanical properties of several recently developed tungsten grades has been investigated. The neutron irradiation campaign has been arranged for a screening purpose and therefore is limited to the neutron fluence (0.2-0.25 dpa in W) relevant for the ITER plasma facing components. At the same time, the neutron exposure covered a span of irradiation temperatures ranging from 600 up to 1000 °C. The investigated grades include: fine-grain tungsten strengthened by W-carbides (W-4wt.% W_2C), fine-grain tungsten strengthened by Zr-carbides (W-0.5% ZrC), W alloyed with 10 at.% chromium and 0.5 at.% yttrium (W-10Cr-0.5Y) and technologically pure W of ITER-specification manufactured by Plansee (Austria). The latter can be considered as "baseline" material implying that its technological production route is well established such that the large-scale procurement may relies on this technology. Development and validation of the advanced grades studied here, so far available at the lab scale, is driven by the harsh operational environment where these materials would function as armour and some preliminary tests suggest a superior performance over the baseline material.

Correspondingly, two essential questions are raised and equivalently assessed for the four tested materials, being: (i) is there any grain growth as a result of the high temperature irradiation? and (ii) is there any loss of the fracture strength as a result of the irradiation? A particular relevance of this screening study comes in the interest to validate the resistance of the selected grades against above mentioned recrystallization and potential loss of the fracture strength at either low or high irradiation temperature. Because the upper test temperature was limited to 600 °C in the hot cells, the determination of the DBTT shift was not possible for some of the grades as their DBTT even in the non-irradiated state was already above 600 °C.

Table 1 provides a concise list of the observed effects of the irradiation on the bending strength and fracture surface. The most common feature is the modification of the fracture mode at low temperature which changes from pure intergranular fracture to the mixed one (trans- and intergranular). Depending on the grade and irradiation temperature, in some cases, the transgranular fracture dominates. In these cases, the loss of the bending strength is also observed except for the W-10Cr-0.5Y grade. No obvious grain growth is observed in either of the tested samples and grades. In the W-WC and W-10Cr-0.5Y grades the void growth is observed after 1000 °C irradiation. In the case of the W-WC grade, this growth apparently explains the increase of the strength. In the case of the W-10Cr-0.5Y grade, a significant increase of strength is associated with the spinodal-like phase decomposition taking place during the irradiation at 1000 °C, resulting in the transformation from an initially single-phase equiaxed-grain microstructure to a vermicular, uniform, ultrafine-grained microstructure of a two-phase mixture. Large cavities with a size below ~10 μm are present as a result of the coalescence of the initial porosity of about 5%, possibly promoted by the phase transformation together with the void formation due to the irradiation. It is expected that a material without initial porosity would undergo even a larger increase of the strength.

Table 1. Summary of the effects of the irradiation on the bending strength and fracture surface.

Material	Fracture strength	Fracture mechanism before -> after irradiation	Microstructural Stability

ITER spec. W, W-IGP	No strength reduction after the irradiation, but shift of the strength curve to a higher temperature (DBTT shift > 100 °C)	Intergranular in reference state changes to the mixture of trans- and intergranular. After irradiation, transgranular fracture prevails.	No grain growth; no pores are observed.
W-4W$_2$C	Reduction of strength at RT after high temperature irradiation. Strength increases at elevated temperature.	Intergranular in reference state changes to the mixture of trans- and intergranular; At T$_{irr}$=800 and 1000 °C the grain cleavage prevails.	Growth of initial pores (and reduction of density) near GBs at T$_{irr}$=1000 °C.
W-10Cr-0.5Y	No reduction after the irradiation, strength especially increases at T$_{irr}$ = 1000 °C	Intergranular in reference state changes to a mixture of trans- and intergranular;	Coalescence of initial pores at T$_{irr}$=1000 °C up to few μm in size; modification of microstructure to a vermicular, uniform, ultrafine-grained two-phase mixture (spinodal phase decomposition).
W-0.5ZrC	Loss of strength below ductile-brittle temperature. DBTT shift = 190 °C.	Intergranular in reference state changes to the mixture of trans- and intergranular; brittle at RT, ductile at 300 °C and above.	No grain growth; Low density of 0.05-0.1 μm pores, possibly decohesion of ZrC particles.

4. Conclusions

Given the presented experimental results and their discussion, two sets of conclusions were formulated, namely technical (specific to measured values) and general (pertinent to fundamental understanding of the irradiation effects in the studied tungsten alloys). Based on the obtained results coming from mechanical tests and microstructural analysis of fracture surfaces, the following specific conclusions can be made:

(i) The DBTT of the ITER specification W baseline material in T-L orientation after the irradiation exceeds 600 °C (irrespective of the irradiation temperature); therefore, its shift could not be established in the current tests. After the irradiation, the fracture strength in the brittle regime remains at the same level or increases to a slightly higher values as compared to the non-irradiated state.

Fracture surface analysis, showing a mixture of the transgranular cleavage and intergranular fracture, does not reveal any considerable grain growth after the irradiation.

(ii) In W-0.5ZrC material, the DBTT increases by 190 °C (becoming 330 °C) after the irradiation at T_{irr}=600 and 800 °C. At T_{irr}=1000 °C, the DBTT increases above 600 °C. The difference in the DBTT shift between 1000 °C and lower irradiation temperature points at the alternation of the damage accumulation. Contrary to the baseline W, the strength of W-0.5ZrC in the brittle regime has dropped below the reference. This result suggests that the high temperature irradiation removes certain microstructural features, which offer high strength and ductility of this material in the non-irradiated state.

Fracture surface analysis does not reveal any considerable grain growth after the irradiation.

(iii) In W-4(W_2C) material, the reduction of the bending strength at T_{irr}=800-1000 °C is observed at RT tests. On the contrary, the strength becomes higher in the high temperature tests i.e. at T_{test}=500 °C. A moderate increase of the strength is observed after the irradiation at 600 °C.

Judging from the fracture surface, no grain growth took place after the irradiation.

The reasons for the alternation in the strength depending on the combination of the irradiation and test temperature require further clarification and dedicated microstructural investigation.

(iv) In W-10Cr-0.5Y material, the bending strength has increased after the neutron irradiation. The increase is remarkably higher at the highest irradiation temperature i.e. T_{irr} = 1000 °C. The microstructural analysis has shown that at T_{irr}=1000 °C the initially single-phase matrix undergone a spinodal-like phase decomposition resulting in a two-phase, uniform, ultrafine-grained microstructure. Besides, coalescence of the pre-existing pores has been probably favored by the phase transformation process. The impact of the initial porosity on the material strength needs further clarification. It is believed that the phase transformation resulting in a spinodal microstructure is in line with a considerable increase of the strength after the irradiation. However, the potential implications of this phase transformation on other properties important for the plasma-facing materials (i.e. sputtering resistance, thermal conductivity, hydrogen retention etc.) are currently unknown and therefore have to be assessed.

In addition to the above listed technical conclusions, we may draw a number of general conclusions important to guide further test programmes on tungsten and its allows for nuclear applications, namely:

- The investigated materials successfully resist massive grain growth (as can be judged from the fracture surfaces) after 1000 °C irradiation at 0.2 dpa.

- High temperature irradiation (~0.3 T_m, T_m – is the melting point) still leads to a considerable shift of the DBTT which is not typical for the steels or copper-alloys, where the irradiation at $0.3 \cdot T_m$ usually leads to mechanical softening (e.g. reduction of the yield stress). This difference can apparently be explained by the transmutation of Re/Os somehow contributing to the enhanced retention of the irradiation defects such as voids and loops.

- Depending on the grade, the change of the strength is found to depend on the irradiation temperature. High irradiation temperature caused stronger changes involving phase transformation in W-10Cr-0.5Y which could be interpreted as co-action of thermodynamic and irradiation effects.

- The main effect of the irradiation on the fracture mechanism was expressed in the appearance of the transgranular cleavage mode, signifying a role of the nano-sized irradiation defects such as voids, loops and probably Re/Os precipitates. Transmission electron microscopy and atom probe tomography is required to clarify whether the accumulation of these irradiation defects differs in the studied grades.

Acknowledgements

References:

[1] M. Rieth, e. al., A brief summary of the progress on the EFDA tungsten materials program, Journal of Nuclear Materials 442(1-3) (2013) S173-S180.

[2] S. Wurster, N. Baluc, M. Battabyal, T. Crosby, J. Du, C. Garcia-Rosales, A. Hasegawa, A. Hoffmann, A. Kimura, H. Kurishita, R.J. Kurtz, H. Li, S. Noh, J. Reiser, J. Riesch, M. Rieth, W. Setyawan, M. Walter, J.H. You, R. Pippan, Recent progress in R&D on tungsten alloys for divertor structural and plasma facing materials, Journal of Nuclear Materials 442(1-3) (2013) S181-S189.

[3] J. Reiser, M. Rieth, B. Dafferner, A. Hoffmann, X.O. Yi, D.E.J. Armstrong, Tungsten foil laminate for structural divertor applications - Analyses and characterisation of tungsten foil, Journal of Nuclear Materials 424(1-3) (2012) 197-203.

[4] S. Antusch, D. Armstrong, B. Britton, L. Commin, J. Gibson, H. Greuner, J. Hoffmann, W. Knabl, G. Pintsuk, M. Rieth, S. Robert, T. Weingaertner, Mechanical and microstructural investigations of tungsten and doped tungsten materials produced via powder injection molding, Nuclear Materials and Energy 3-4 (2015) 22-31.

[5] J.W. Coenen, S. Antusch, M. Aumann, W. Biel, J. Du, J. Engels, S. Heuer, A. Houben, T. Hoeschen, B. Jasper, F. Koch, J. Linke, A. Litnovsky, Y. Mao, R. Neu, G. Pintsuk, J. Riesch, M. Rasinski, J. Reiser, M. Rieth, A. Terra, B. Unterberg, T. Weber, T. Wegener, J.H. You, C. Linsmeier, Materials for DEMO and reactor applications-boundary conditions and new concepts, Physica Scripta T167 (2016).

[6] C. Linsmeier, M. Rieth, J. Aktaa, T. Chikada, A. Hoffmann, J. Hoffmann, A. Houben, H. Kurishita, X. Jin, M. Li, A. Litnovsky, S. Matsuo, A. von Muller, V. Nikolic, T. Palacios, R. Pippan, D. Qu, J. Reiser, J. Riesch, T. Shikama, R. Stieglitz, T. Weber, S. Wurster, J.H. You, Z. Zhou, Development of advanced high heat flux and plasma-facing materials, Nuclear Fusion 57(9) (2017).

[7] C. Yin, D. Terentyev, T. Pardoen, A. Bakaeva, R. Petrov, S. Antusch, M. Rieth, M. Vilemova, J. Matejicek, T. Zhang, Tensile properties of baseline and advanced tungsten grades for fusion applications, Int J Refract Met H 75 (2018) 153-162.

[8] C. Yin, D. Terentyev, T. Zhang, S. Nogami, S. Antusch, C.C. Chang, R.H. Petrov, T. Pardoen, Ductile to brittle transition temperature of advanced tungsten alloys for nuclear fusion applications deduced by miniaturized three-point bending tests, Int J Refract Met H 95 (2021).

[9] C. Bonnekoh, A. Hoffmann, J. Reiser, The brittle-to-ductile transition in cold rolled tungsten: On the decrease of the brittle-to-ductile transition by 600 K to-65 degrees C, Int J Refract Met H 71 (2018) 181-189.

[10] B. Gludovatz, S. Wurster, A. Hoffmann, R. Pippan, Fracture toughness of polycrystalline tungsten alloys, Int J Refract Met H 28(6) (2010) 674-678.

[11] Q. Wei, L.J. Kecskes, Effect of low-temperature rolling on the tensile behavior of commercially pure tungsten, Mat Sci Eng a-Struct 491(1-2) (2008) 62-69.

[12] G. Pintsuk, Tungsten as plasma facing material, Comprehensive Nuclear Materials 4 (2012) 551-581.

[13] U.M. Ciucani, A. Thum, C. Devos, W. Pantleon, Recovery and recrystallization kinetics of differently rolled, thin tungsten plates in the temperature range from 1325 degrees C to 1400 degrees C, Nuclear Materials and Energy 20 (2019).

[14] G. Pintsuk, S. Antusch, T. Weingaertner, M. Wirtz, Recrystallization and composition dependent thermal fatigue response of different tungsten grades, Int J Refract Met H 72 (2018) 97-103.

[15] E. Lassner, W.D. Schubert, Tungsten - Properties, Chemistry, Technology of the Element, Alloys, and Chemical Compounds (Kluwer Academic / Plenum Publishers) (1999).

[16] J. Reiser, J. Hoffmann, U. Jantsch, M. Klimenkov, S. Bonk, C. Bonnekoh, A. Hoffmann, T. Mrotzek, M. Rieth, Ductilisation of tungsten (W): On the increase of strength AND room-temperature tensile ductility through cold-rolling, Int J Refract Met H 64 (2017) 261-278.

[17] C. Ren, Z.Z. Fang, M. Koopman, B. Butler, J. Paramore, S. Middlemas, Methods for improving ductility of tungsten - A review, Int J Refract Met H 75 (2018) 170-183.

[18] L. Tanure, A. Bakaeva, A. Dubinko, D. Terentyev, K. Verbeken, Effect of annealing on microstructure, texture and hardness of ITER-specification tungsten analyzed by EBSD, vickers micro-hardness and nano-indentation techniques, Journal of Nuclear Materials 524 (2019) 191-199.

[19] J. Reiser, C. Bonnekoh, T. Karcher, W. Pfleging, D. Weygand, A. Hoffmann, Recrystallisation towards a single texture component in heavily cold rolled tungsten (W) sheets and its impact on micromechanics, Int J Refract Met H 86 (2020).

[20] Y. Kim, K.H. Lee, E.P. Kim, D.I. Cheong, S.H. Hong, Fabrication of high temperature oxides dispersion strengthened tungsten composites by spark plasma sintering process, Int J Refract Met H 27(5) (2009) 842-846.

[21] Y. Kitsunai, H. Kurishita, H. Kayano, Y. Hiraoka, T. Igarashi, T. Takida, Microstructure and impact properties of ultra-fine grained tungsten alloys dispersed with TiC, Journal of Nuclear Materials 271 (1999) 423-428.

[22] S.T. Lang, Q.Z. Yan, N.B. Sun, X.X. Zhang, L. Deng, Y.J. Wang, Microstructure, basic thermal-mechanical and Charpy impact properties of W-0.1 wt.% TiC alloy via chemical method, Journal of Alloys and Compounds 660 (2016) 184-192.

[23] S. Novak, M. Kocen, A.S. Zavagnik, A. Galatanu, M. Galatanu, S. Tarancon, E. Tejado, J.Y. Pastor, P. Jenus, Beneficial effects of a WC addition in FAST-densified tungsten, Mat Sci Eng a-Struct 772 (2020).

[24] P. Jenus, A. Ivekovic, M. Kocen, A. Sestan, S. Novak, W2C-reinforced tungsten prepared using different precursors, Ceram Int 45(6) (2019) 7995-7999.

[25] D. Maisonnier, I. Cook, S. Pierre, B. Lorenzo, D.P. Luigi, G. Luciano, N. Prachai, P. Aldo, DEMO and fusion power plant conceptual studies in Europe, Fusion Engineering and Design 81(8-14) (2006) 1123-1130.

[26] M.R. Gilbert, T. Eade, C. Bachmann, U. Fischer, N.P. Taylor, Activation, decay heat, and waste classification studies of the European DEMO concept, Nuclear Fusion 57(4) (2017).

[27] F. Koch, S. Koppl, H. Bolt, Self passivating W-based alloys as plasma-facing material, Journal of Nuclear Materials 386-88 (2009) 572-574.

[28] T. Wegener, F. Klein, A. Litnovsky, M. Rasinski, J. Brinkmann, F. Koch, C. Linsmeier, Development of yttrium-containing self-passivating tungsten alloys for future fusion power plants, Nuclear Materials and Energy 9 (2016) 394-398.

[29] A. Calvo, C. Garcia-Rosales, F. Koch, N. Ordas, I. Iturriza, H. Greuner, G. Pintsuk, C. Sarbu, Manufacturing and testing of self-passivating tungsten alloys of different composition, Nuclear Materials and Energy 9 (2016) 422-429.

[30] A. Calvo, K. Schlueter, E. Tejado, G. Pintsuk, N. Ordas, I. Iturriza, R. Neu, J.Y. Pastor, C. Garcia-Rosales, Self-passivating tungsten alloys of the system W-Cr-Y for high temperature applications, Int J Refract Met H 73 (2018) 29-37.

[31] C. Garcia-Rosales, P. Lopez-Ruiz, S. Alvarez-Martin, A. Calvo, N. Ordas, F. Koch, J. Brinkmann, Oxidation behaviour of bulk W-Cr-Ti alloys prepared by mechanical alloying and HIPing, Fusion Engineering and Design 89(7-8) (2014) 1611-1616.

[32] F. Klein, T. Wegener, A. Litnovsky, M. Rasinski, X.Y. Tan, J. Gonzalez-Julian, J. Schmitz, M. Bram, J.W. Coenen, C. Linsmeier, Oxidation resistance of bulk plasma- facing tungsten alloys, Nuclear Materials and Energy 15 (2018) 226-231.

[33] A. Litnovsky, T. Wegener, F. Klein, C. Linsmeier, M. Rasinski, A. Kreter, B. Unterberg, J.W. Coenen, H. Du, J. Mayer, C. Garcia-Rosales, A. Calvo, N. Ordas, Smart tungsten alloys as a material for the first wall of a future fusion power plant, Nuclear Fusion 57(6) (2017).

[34] G. Federici, W. Biel, M.R. Gilbert, R. Kemp, N. Taylor, R. Wenninger, European DEMO design strategy and consequences for materials, Nuclear Fusion 57(9) (2017).

[35] J. Knaster, S. Chel, U. Fischer, F. Groeschel, R. Heidinger, A. Ibarra, G. Micciche, A. Moslang, M. Sugimoto, E. Wakai, IFMIF, a fusion relevant neutron source for material irradiation current status, Journal of Nuclear Materials 453(1-3) (2014) 115-119.

[36] D. Bernardi, F. Arbeiter, M. Cappelli, U. Fischer, A. Garcia, R. Heidinger, W. Krolas, F. Martin-Fuertes, G. Micciche, A. Munoz, F.S. Nitti, M. Perez, T. Firma, K. Tian, A. Ibarra, I.-D. Team, Towards the EU fusion-oriented neutron source: The preliminary engineering design of IFMIF-DONES, Fusion Engineering and Design 146 (2019) 261-268.

[37] L.M. Garrison, Y. Katoh, J.W. Geringer, M. Akiyoshi, X. Chen, M. Fukuda, A. Hasegawa, T. Hinoki, X.X. Hu, T. Koyanagi, E. Lang, M. McAlister, J. McDuffee, T. Miyazawa, C. Parish, E. Proehl, N. Reid, J. Robertson, H. Wang, PHENIX US-Japan Collaboration Investigation of Thermal and Mechanical Properties of Thermal Neutron-Shielded Irradiated Tungsten, Fusion Science and Technology 75(6) (2019) 499-509.

[38] A. Hasegawa, M. Fukuda, K. Yabuuchi, S. Nogami, Neutron irradiation effects on the microstructural development of tungsten and tungsten alloys, Journal of Nuclear Materials 471 (2016) 175-183.

[39] J.H. You, E. Visca, T. Barrett, B. Boswirth, F. Crescenzi, F. Domptail, M. Fursdon, F. Gallay, B.E. Ghidersae, H. Greunera, M. Li, A.V. Muller, J. Reiser, M. Richou, S. Roccella, C. Vorpahl, European divertor target concepts for DEMO: Design rationales and high heat flux performance, Nuclear Materials and Energy 16 (2018) 1-11.

[40] D. Terentyev, C. Yin, A. Dubinko, C.C. Chang, J.H. You, Neutron irradiation hardening across ITER diverter tungsten armor, Int J Refract Met H 95 (2021).

[41] X.X. Hu, T. Koyanagi, M. Fukuda, N.A.P.K. Kumar, L.L. Snead, B.D. Wirth, Y. Katoh, Irradiation hardening of pure tungsten exposed to neutron irradiation, Journal of Nuclear Materials 480 (2016) 235-243.

[42] H. Gietl, T. Koyanagi, X.X. Hu, M. Fukuda, A. Hasegawa, Y. Katoh, Neutron irradiation-enhanced grain growth in tungsten and tungsten alloys, Journal of Alloys and Compounds 901 (2022).

[43] M. Wirtz, J. Linke, T. Loewenhoff, G. Pintsuk, I. Uytdenhouwen, Thermal shock tests to qualify different tungsten grades as plasma facing material, Physica Scripta T167 (2016) 014015.

[44] D. Terentyev, C.C. Chang, C. Yin, A. Zinovev, X. He, Neutron irradiation effects on mechanical properties of ITER specification tungsten, Tungsten 3 (2021) 415–433.

[45] E. Gaganidze, A. Chauhan, H.-C. Schneider, D. Terentyev, G. Borghmans, J. Aktaa, Fracture-mechanical properties of neutron irradiated ITER specification tungsten, Journal of Nuclear Materials 547 (2021) 152761.

[46] D. Terentyev, C. Yin, A. Dubinko, C.C. Chang, J.H. You, Neutron irradiation hardening across ITER diverter tungsten armor, International Journal of Refractory Metals and Hard Materials 95 (2021) 105437.

[47] Z.M. Xie, R. Liu, S. Miao, X.D. Yang, T. Zhang, X.P. Wang, Q.F. Fang, C.S. Liu, G.N. Luo, Y.Y. Lian, X. Liu, Extraordinary high ductility/strength of the interface designed bulk W-ZrC alloy plate at relatively low temperature, Sci Rep-Uk 5 (2015).

[48] Z.M. Xie, R. Liu, Q.F. Fang, T. Zhang, Y. Jiang, X.P. Wang, C.S. Liu, Microstructure and Mechanical Properties of Nano-Size Zirconium Carbide Dispersion Strengthened Tungsten Alloys Fabricated by Spark Plasma Sintering Method, Plasma Sci Technol 17(12) (2015) 1066-1071.

[49] X.D. Yang, Z.M. Xie, S. Miao, R. Liu, W.B. Jiang, T. Zhang, X.P. Wang, Q.F. Fang, C.S. Liu, G.N. Luo, X. Liu, Tungsten-zirconium carbide-rhenium alloys with extraordinary thermal stability, Fusion Engineering and Design 106 (2016) 56-62.

[50] E. Sal, C. Garcia-Rosales, I. Iturriza, I. Andueza, N. Burgo, High temperature microstructural stability of self-passivating W-Cr-Y alloys for blanket first wall application, Fusion Engineering and Design 146 (2019) 1596-1599.

[51] S.V. Nagender Naidu, A.M. Sriramamurthy, P.R. Rao, The Cr-W (Chromium-Tungsten) System, Bull. Alloy Phase Diagrams 5 (1984) 289.

[52] F.J. den Broeder, Interface reaction and a special form of grain boundary diffusion in the Cr-W system, Acta Metall. 20 (1972) 319-332.

[53] E. Sal, C. Garcia-Rosales, K. Schlueter, K. Hunger, M. Gago, M. Wirtz, A. Calvo, I. Andueza, R. Neu, G. Pintsuk, Microstructure, oxidation behaviour and thermal shock resistance of self-passivating W-Cr-Y-Zr alloys, Nuclear Materials and Energy 24 (2020).

[54] E. Gaganidze, A. Chauhan, H.-C. Schneider, D. Terentyev, G. Borghmans, J. Aktaa, Fracture-mechanical properties of neutron irradiated ITER specification tungsten, J Nucl Mater 152761.

[55] C. Yin, D. Terentyev, T. Zhang, R.H. Petrov, T. Pardoen, Impact of neutron irradiation on the strength and ductility of pure and ZrC reinforced tungsten grades, J Nucl Mater 537 (2020) 152226.

[56] G. Bonny, M. Konstantinovic, A. Bakaeva, C. Yin, N. Castin, K. Mergia, V. Chatzikos, S. Dellis, T. Khvan, A. Bakaev, Trends in vacancy distribution and hardness of high temperature neutron irradiated single crystal tungsten, Acta Materialia 198 (2020) 1-9.

[57] D. Pelowitz, J. Durkee, J. Elson, M. Fensin, M. James, R. Johns, G. McKinney, S. Mashnik, L. Waters, T. Wilcox, MCNPX 2.7. 0 Extensions, Los Alamos National Laboratory, 2011.

[58] A. Stankovskiy, G. Van den Eynde, L. Fiorito, ALEPH V.2.7, A Monte Carlo Burn-Up Code, SCK•CEN, 2018.

[59] JEFF Scientific Working group, The joint evaluated fission and fusion nuclear data library, JEFF-3.3, Nuclear Energy Agency, 2017.

[60] D.A. Brown, M. Chadwick, R. Capote, A. Kahler, A. Trkov, M. Herman, A. Sonzogni, Y. Danon, A. Carlson, M. Dunn, ENDF/B-VIII. 0: the 8th major release of the nuclear reaction data library with CIELO-project cross sections, new standards and thermal scattering data, Nuclear Data Sheets 148 (2018) 1-142.

[61] A.Y. Konobeyev, U. Fischer, Y.A. Korovin, S. Simakov, Evaluation of effective threshold displacement energies and other data required for the calculation of advanced atomic displacement cross-sections, Nuclear Energy and Technology 3(3) (2017) 169-175.

[62] A. Bakaev, D. Terentyev, A. Zinovev, C. Chang, C. Yin, Application of sub-miniaturized bending tests to extract tensile properties from neutron-irradiated metallic alloys, Journal of Nuclear Materials 558 (2022) 153320.

[63] C. Yin, D. Terentyev, T. Pardoen, R. Petrov, Z.F. Tong, Ductile to brittle transition in ITER specification tungsten assessed by combined fracture toughness and bending tests analysis, Mat Sci Eng a-Struct 750 (2019) 20-30.

[64] D.H. Lassila, F. Magness, D. Freeman, Ductile-Brittle Transition Temperature Testing of Tungsten Using the Three-Point Bend Test, Report Lawrence Livermore National Laboratory UCRL-ID-108258 (1991).

[65] A. Dubinko, D. Terentyev, A. Bakaeva, K. Verbeken, M. Wirtz, M. Hernandez-Mayoral, Evolution of plastic deformation in heavily deformed and recrystallized tungsten of ITER specification studied by TEM, Int. Journal of Refractory Metals and Hard Materials 66 (2017) 105-115.

[66] C. Yin, D. Terentyev, T. Pardoen, A. Bakaeva, R. Petrov, S. Antusch, M. Rieth, M. Vilemova, J. Matejicek, T. Zhang, Tensile properties of baseline and advanced tungsten grades for fusion applications, Int. J. Refract. Met. Hard Mater. 75 (2018) 153-162.

[67] Z.M. Xie, R. Liu, S. Miao, X.D. Yang, T. Zhang, X.P. Wang, Q.F. Fang, C.S. Liu, G.N. Luo, Y.Y. Lian, X. Liu, Extraordinary high ductility/strength of the interface designed bulk W-ZrC alloy plate at relatively low temperature, Scientific Reports 5 (2015) 1-11.

[68] A. Dubinko, C. Yin, D. Terentyev, A. Zinovev, M. Rieth, S. Antusch, M. Vilemova, J. Matejicek, T. Zhang, Plastic deformation in advanced tungsten-based alloys for fusion applications studied by mechanical testing and TEM, Int J Refract Met H in press, https://doi.org/10.1016/j.ijrmhm.2020.105409 (2020) 105409.

[69] D.E. Porter, The decomposition of tungsten-chromium solid solution, Acta Metall. 15 (1967) 721-726.

[70] J.A. Hanna, I. Baker, M.W. Wittmann, P.R. Munroe, A new high-strength spinodal alloy, J Mater Res 20(4) (2005) 791-795.

[71] C. Yin, D. Terentyev, T. Pardoen, R. Petrov, Z. Tong, Ductile to brittle transition in ITER specification tungsten assessed by combined fracture toughness and bending tests analysis, Mater. Sci. Eng. A 750 (2019) 20-30.

[72] D.H. Lassila, F. Magness, D. Freeman, Ductile-Brittle Transition Temperature Testing of Tungsten Using the Three-Point Bend Test, Report Lawrence Livermore National Laboratory, 1991.

[73] H.E. Exner, G. Petzow, A Critical Assessment of Porosity coarsening During Solid State Sintering, Adv. Sci. Tech. 45 (2006) 539-548.

[74] R. R.C., L. R.L., M. J., Voids in irradiated tungsten and molybdenum, Journal of Nuclear Materials 33 (1969) 324-327.